

# Stability analysis of improved confinement discharges: internal transport barriers in Tore Supra and radiative improved mode in TEXTOR

C. Bourdelle<sup>a</sup>, X. Garbet, G.T. Hoang, J. Ongena<sup>1</sup> and R.V. Budny<sup>2</sup>

Association Euratom–CEA, CEA/DSM/DRFC, CEA Cadarache, Saint-Paul-lez-Durance, France

<sup>1</sup> Laboratoire de Physique des Plasmas/Laboratorium voor Plasmafysica, Association Euratom–Etat belge/Associate Euratom–Belgische Staat, Ecole royale militaire/Koninklijke Militaire School, Brussels, Belgium

<sup>2</sup> Princeton Plasma Physics Laboratory, Princeton University, Princeton, New Jersey, USA

E-mail: cbourdelle@pppl.gov

Received 2 April 2001, accepted for publication 7 December 2001

Published 18 July 2002

Online at [stacks.iop.org/NF/42/892](http://stacks.iop.org/NF/42/892)

## Abstract

Results of stability analysis are presented for two types of plasma with good confinement: internal transport barriers (ITBs) on Tore Supra and the radiative improved (RI) mode on TEXTOR. The stability analysis has been performed with an electrostatic linear gyrokinetic code, evaluating the growth rates of microinstabilities. The code developed, KINEZERO, is aimed at systematic microstability analysis. Therefore the trade-off between having perfect quantitative agreement and minimizing computation time is made in favour of the latter. In the plasmas analysed, it is found that the onset of the confinement improvement involves a trigger. For the ITB discharges, negative magnetic shear is involved, whereas for the RI discharges, the triggering role is played by the increase of the impurity concentration. Once the improved confinement is triggered, the simultaneous increases of temperature and density gradients imply an increase in both the growth rate and the rotation shearing rate. The rotation shear is found to be high enough to maintain an improved confinement through the stabilization of the large scale modes.

**PACS numbers:** 52.55.Fa, 52.25.Fi, 52.55.-s

## 1. Introduction

The achievement of plasmas with good confinement properties is an important field of research for magnetic fusion devices. Several promising ways to achieve such high performance regimes have been intensively investigated in many tokamak devices: TFTR [1], DIII-D [2], JT-60U [3], JET [4], TEXTOR [5], FTU [6], ASDEX Upgrade [7] and Tore Supra [8]. One purpose of these experiments is to minimize the power threshold needed to obtain improved confinement regimes. Another goal is to determine the conditions for a steady state regime. Regarding these issues, understanding the mechanisms which trigger and maintain a state with low turbulent transport is of prime importance. The study of a

turbulent plasma requires non-linear simulations. Nowadays non-linear simulations are still too time consuming to be routinely performed for each discharge of interest [9]. Conversely, a linear stability calculation is much faster and gives some useful information by providing the growth rates of the microinstabilities. A reliable linear stability code must be based on a gyrokinetic model [10, 11] or on a gyro-Landau fluid model [12–14], since a fluid calculation cannot correctly provide the instability threshold. However, a full gyrokinetic calculation, yielding growth rates for each toroidal wavenumber and magnetic surface, requires a large amount of computation time. In order to provide results on a day to day basis, a simplified code is therefore required. Such a code, called KINEZERO, based on a variational principle, has recently been developed at Tore Supra. It has been used to analyse various types of improved confinement plasma.

<sup>a</sup> Present address: Princeton Plasma Physics Laboratory, Princeton University, PO Box 451, Princeton, NJ 08543, USA.

The first application deals with the Tore Supra plasmas, characterized by a central negative magnetic shear ( $s$ ), which exhibit internal transport barriers (ITBs) on both electron and ion channels. The second study addresses the TEXTOR radiative improved (RI) mode, which is characterized by good confinement at high density and high fraction of radiated power. These analyses show that the improvement of the confinement is triggered by a negative value of  $s$  in the ITB case and by impurity seeding in the RI case. In these two kinds of plasma, we find that the improved confinement is probably maintained by an increase of the  $\mathbf{E} \times \mathbf{B}$  shearing rate ( $\gamma_E$ ).

This article is organized as follows. The stability code is described in section 2, with more details reported in the appendix. The stability analyses of the Tore Supra ITB discharges are presented in section 3. In section 4, the TEXTOR RI discharges are analysed. Finally a summary is given in section 5.

## 2. Outline of the code KINEZERO

To characterize microinstabilities we have developed an electrostatic linear gyrokinetic code, KINEZERO (see the appendix). This code evaluates the growth rates ( $\gamma$ ), which are the imaginary parts of the eigenmode pulsations ( $\omega$ ). The calculation is performed for each toroidal wavenumber ( $n$ ) on a set of magnetic surfaces. The density perturbations, induced by the perturbed electrostatic potential, are computed by linearizing the Vlasov equation, and the coherence is expressed by the electroneutrality constraint. For a given magnetic surface (radial position  $r$ ) and at  $n$  fixed, the poloidal wavenumber ( $m$ ) is constrained by the safety factor:  $q = -m/n$ . In our calculation, the magnetic perturbations are neglected. This approximation is valid for very low values of beta:  $\beta < m_e/m_i$  ( $m_e$  and  $m_i$  being the electron and ion masses). Here  $\beta$  is defined as the ratio of the total kinetic pressure  $P$  over the total magnetic pressure  $B^2/2\mu_0$ . The actual values of  $\beta$  in Tore Supra and TEXTOR are larger than this limit. However, these  $\beta$  values are still well below the threshold for destabilizing kinetic ballooning modes [15]. Furthermore,  $\beta$  is globally stabilizing for the usual branches of drift waves [16]. Our choice is therefore conservative since the growth rates are overestimated. The effect of collisions is also neglected. This approximation is not valid when the effective collision frequency becomes of the same order as the vertical drift frequency of trapped electrons. In order to reduce the computation time, we also use a simplified formulation of the equations. The ballooning representation at the lowest order is used to represent the perturbed electric field  $\tilde{\phi}$  as follows:

$$\begin{aligned} \tilde{\phi}(r, \theta, \varphi, t) &= \sum_{mn, \omega} \tilde{\phi}_{mn, \omega}(r) e^{i(m\theta + n\varphi - \omega t)} \\ &= \sum_{n, \omega} \int \frac{d\theta_0}{2\pi} \sum_{l=-\infty}^{+\infty} \hat{\phi}_{n\omega\theta_0}(\theta + 2\pi l) \\ &\quad \times \exp[i\{n(\varphi - q(r)(\theta + 2\pi l - \theta_0)) - \omega t\}]. \end{aligned} \quad (1)$$

The ballooning angle is restricted to  $\theta_0 = 0$ , which usually corresponds to the most unstable value with respect to the interchange instability. This procedure allows us to reduce the determination of the eigenmodes to a 1-D problem, instead of 2-D. The ballooning representation

is valid if the gradient lengths of equilibrium quantities ( $L_n = -n/\nabla n$ ,  $L_T = -T/\nabla T$ ) are larger than the distance between two adjacent resonant surfaces ( $d = |1/n \partial_r q|$ ). This representation does not give access to the stabilizing effect of  $\gamma_E$ . To take this effect into account in our calculation, we have used a heuristic criterion. Moreover, the ballooning representation does not describe the zero  $s$  configuration correctly, since in this case  $d$  is infinite and cannot be smaller than the gradient lengths.

To speed up the calculations, we recast the electroneutrality constraint under a variational form [17], and we use a trial function for the fluctuating electrostatic potential. This trial function is chosen to be the most unstable exact solution obtained in the fluid limit. This Gaussian function is also obtained by most of the kinetic calculations [10].

Combining the perturbed Vlasov equation with the variational form of electroneutrality constraint, one obtains the following equation for  $\omega$ :

$$\mathcal{D}(\omega) = \sum_s \frac{n_s Z_s^2}{T_s} [1 - \mathcal{L}_{ts}(\omega) - \mathcal{L}_{ps}(\omega)] = 0 \quad (2)$$

where  $n_s$ ,  $Z_s$  and  $T_s$  are, respectively, the density, charge number and temperature of the species  $s$ . The species treated here are electrons and two types of ion, typically the main ions and one kind of impurity. The functional expressions for the trapped ( $\mathcal{L}_{ts}$ ) and passing ( $\mathcal{L}_{ps}$ ) particles are given in the appendix by equations (24) and (27).

These functionals are multiple integrals of rapidly varying complex variable functions. We therefore need an efficient method to find the solutions of this equation. We use a generalized Nyquist method developed by Davies [18] and extended by Brunner *et al* [19]. The method consists in using the argument principle and the residues theorem. In this way, knowing the values of  $\mathcal{D}(\omega)$  over a contour  $\mathcal{C}$  yields the zeros of  $\mathcal{D}$  in the domain enclosed by  $\mathcal{C}$ . In order to obtain all the unstable solutions, we scan the upper part of the  $\omega$  complex plane with several contours. The maximum value along the imaginary axis is given by an estimate of the growth rate calculated using fluid equations. The minimum value has to be positive and can be chosen as small as needed. Once we have determined the eigenvalues using this method, we refine their localization using Newton's method. The solutions are classified in decreasing order of their imaginary part ( $\gamma$ ). This is done for each pair ( $n, r/a$ ). The stability analyses are performed using the growth rate of the most unstable mode for each ( $n, r/a$ ):  $\gamma^{max}(n, r/a)$ .

The inputs used in the code are the measured profiles: the electron and ion temperature profiles ( $T_e(r)$ ,  $T_i(r)$ ); the density profiles of electrons, ions and one impurity ( $n_e(r)$ ,  $n_i(r)$ ,  $n_z(r)$ ); the safety factor profile ( $q(r)$ ); the major and minor radii  $R$  and  $a$ ; and the toroidal magnetic field ( $B_T$ ). Here the magnetic configuration is supposed to be concentric circular, which is the case for Tore Supra and TEXTOR. In this version, the Shafranov shift is neglected, consistent with the electrostatic assumption. From this set of information we evaluate the gradient lengths, the magnetic shear, the trapped particle fraction, the Larmor radii and the banana widths.

A typical result for a standard L mode Tore Supra plasma ( $I_p = 1.4$  MA,  $T_e(0) = 4$  keV,  $T_i(0) = 3$  keV,  $n_e(0) = 6 \times$

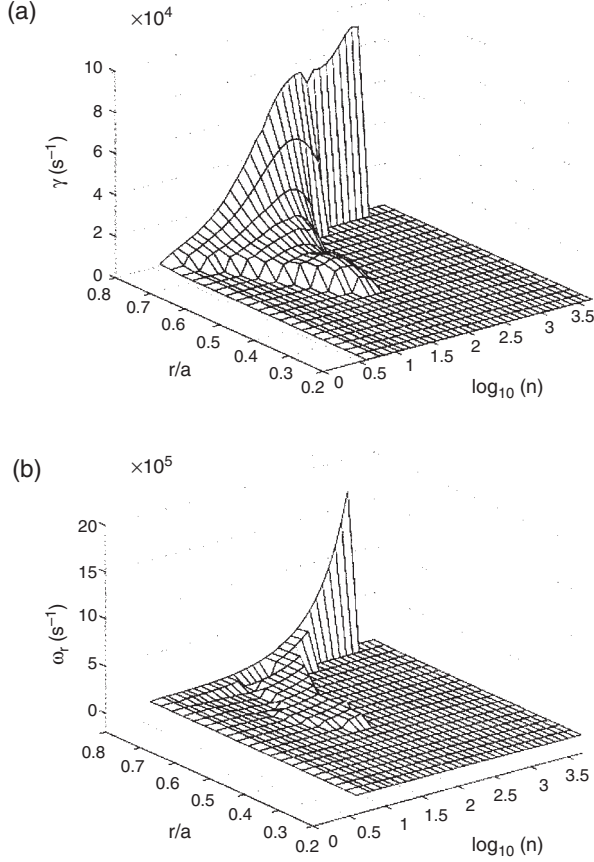


**Figure 1.** Standard L mode discharge performed at  $I_p = 1.5$  MA,  $n_e(0) = 7 \times 10^{19} \text{ m}^{-3}$ , with 6 MW of ICRH. (a) Growth rates for  $5 \leq n \leq 5 \times 10^3$ ,  $0.2 \leq r/a \leq 0.8$ . (b) Real frequencies for  $5 \leq n \leq 5 \times 10^3$ ,  $0.2 \leq r/a \leq 0.8$ .

$10^{19} \text{ m}^{-3}$ ) is shown in figure 1. This result was obtained after 5 h of computational time on a single Dec Alpha workstation. Figure 1 shows that the modes with  $n$  ranging between 10 and 100 are dominant in the region  $0.4 < r/a < 0.8$ . This corresponds to a mixture of the ion modes driven by the ion temperature gradient (ITG) and the trapped electron modes (TEMs). For wavenumbers larger than 100 ( $k_\theta \rho_i \gg 1$ ,  $\rho_i$  being the ion Larmor radius), only the passing electron modes driven by the electron temperature gradient (ETG) are potentially unstable. In the following, we will use the KINEZERO code to identify the key parameters leading to the improvement of confinement in the experiments of Tore Supra and TEXTOR.

### 3. Stability analysis of the ITB discharges with ion cyclotron resonance heating on Tore Supra

These experiments have been carried out at:  $I_p = 1.2\text{--}1.4$  MA,  $B_T = 3.6$  T,  $R = 2.4$  m,  $a = 0.75$  m and  $n_e(0)$  up to  $7 \times 10^{19} \text{ m}^{-3}$ . The scheme of ion cyclotron resonance heating (ICRH) in hydrogen minority was used as the only auxiliary heating. The scenario consists in performing a non-monotonic  $q$  profile before coupling the ICRH power ( $P_{ICRH} < 4$  MW) [8]. A hollow  $q$  profile was produced by freezing the diffusion of resistive current during a fast

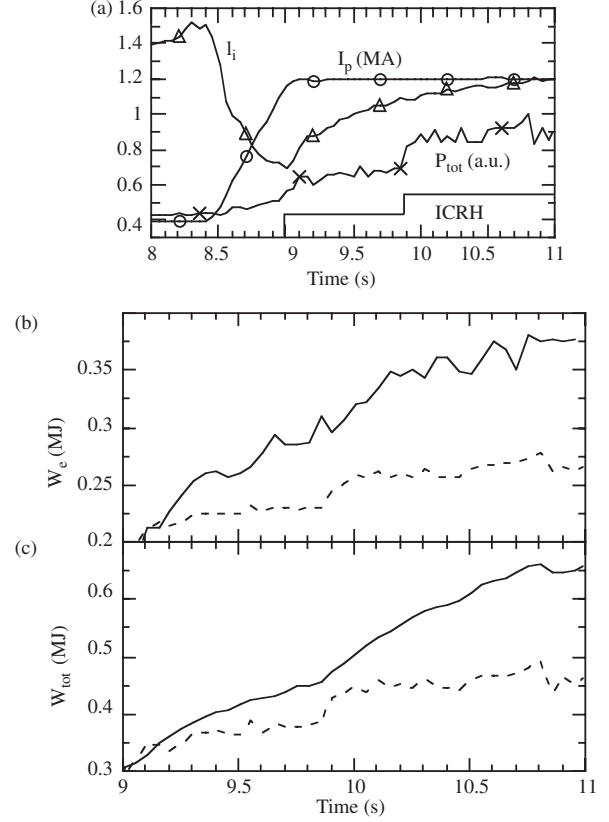


**Figure 2.** ITB/ICRH discharge (TS25196) on Tore Supra at  $n_e(0) = 6.5 \times 10^{19} \text{ m}^{-3}$ , with preformed central negative magnetic shear produced by a fast ramp-up. (a) Plasma current ( $I_p$ ), self-inductance ( $I_i$ ) and total power ( $P_{ICRH} = 2$  MW/4 MW). (b) Electron energy (solid curve) and Rebut-Lallia-Watkins L mode prediction (dashed curve). (c) Stored thermal energy (solid curve) and L mode ITER prediction (dashed curve).

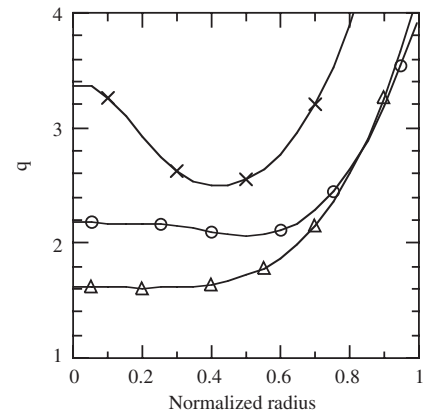


**Figure 3.** Evolution of  $q$  profile for shot TS25196, shown in figure 2, before ( $t = 8.7$  s, crosses) and during ( $t = 9.1$  s, circles, and  $9.8$  s, triangles) ICRH application.

ramp-up ( $dI_p/dt = 1.6 \text{ MA s}^{-1}$ ) from a steady state flat-top  $I_p = 0.4$  MA (figure 2(a)). During the  $I_p$  ramp-up, a reversed central magnetic shear was observed, as shown in figure 3. The transient reversed central magnetic shear was maintained on the 1.2 MA flat-top when ICRH was applied (at  $t = 9$  s) for about 0.2 s ( $t = 9\text{--}9.2$  s). At  $t = 8.7$  s, where  $s$  becomes negative, the measurements of density

fluctuations by a heterodyne CO<sub>2</sub> laser scattering diagnostic for  $k = 8 \text{ cm}^{-1}$  display a significant reduction [20]. This reduction of fluctuations is consistent with the observation of an increase in the electron energy, which exceeds the L mode value by a factor of about 1.4 (figure 2(b)). Also, the global energy confinement time is found to be higher than that of the L mode by a factor  $H$  of 1.4 (figure 2(c)). As shown in figure 4(a), the electron pressure profile clearly increases within  $r/a < 0.6$ . One can see that the pressure profile obtained with  $P_{ICRH} = 2 \text{ MW}$  (2.7 MW total power) is quite the same as that of the L mode performed with 4 MW (4.5 MW total power). Both the low level of turbulence and the improvement of the confinement remain during the ICRH application (9–11 s), whereas the hollow  $q$  profile relaxes towards a monotonic shape. Transport analysis also shows a decrease in the effective transport coefficient ( $\chi_{eff}$ ) inside the barrier (figure 4(b)).

Two time slices are chosen for stability analysis:  $t = 9.1 \text{ s}$  ( $s = -0.1$ ) and  $t = 9.8 \text{ s}$  ( $s = 0.2$ ). The radial profiles of the normalized gradient lengths  $A_n = R/L_n$  and  $A_T = R/L_T$ , as well as the magnetic shear  $s$ , are shown in figure 5. The growth rate spectrum at  $t = 9.1 \text{ s}$  at  $r/a = 0.4$  is shown in figure 6 (solid curve). In order to quantify the effect of a locally

negative magnetic shear, we have computed  $\gamma$  by assuming a monotonic  $q$  profile:  $s = 0.2$  instead of the measured value of  $-0.1$ , as shown in figure 6 (dashed curve).  $\gamma$  is significantly reduced (by a factor of  $< 3$ ) with a negative value of  $s$ . This is consistent with the reduction of density fluctuations observed at  $t = 9.1 \text{ s}$ , where  $s$  becomes negative. At  $t = 9.8 \text{ s}$ , the radial profile of  $\gamma_{max}$  over each  $n$  spectrum is found to increase in the region  $0.2 < r/a < 0.6$  (i.e. inside the ITB), as shown in figure 7. This is due to the increase of the density and temperature gradients and the monotonic  $q$  profile. This result is not consistent with the observed reductions of turbulence and  $\chi_{eff}$ . This is due to the fact that the stabilizing effect of  $\gamma_E$  is not included in our code. In order to quantify this effect, we have computed  $\gamma_E$  with the following formula [21]:

$$\gamma_E = \frac{r}{q} \left| \frac{d}{dr} \left( \frac{q}{r} \frac{E_r}{B} \right) \right| \quad (3)$$

since the measurement of the radial electric field was not available in the experiments considered. We evaluate  $E_r$  from the ambipolarity constraint on ripple losses [22–26] (ripple up to 7% on Tore Supra). The trapped particles in the ripple wells undergo vertical drift, collisions and  $\mathbf{E} \times \mathbf{B}$  drift. They are lost unless the collisions detrap them. Neglecting the flux of lost thermal electrons (since the ion collision frequency is much weaker than that of electrons), we obtain the following expression for  $E_r$ :

$$E_r \simeq \frac{T_i}{Z_i n_i} \frac{\partial n_i}{\partial r} + 3.5 \frac{1}{Z_i} \frac{\partial T_i}{\partial r}. \quad (4)$$

Equation (4) has been verified for ohmic discharges, in which  $E_r$  was found to agree with the measured toroidal rotation [27]. For the present case,  $E_r$  is probably underestimated, since we neglect the contribution of fast particle losses generated by ICRH. Combining equations (3) and (4) gives a maximum value of  $\gamma_E$  at normalized radius  $r/a = 0.6$ , i.e. at approximately the position of the foot of the barrier. The time trace of this maximum value is plotted together with  $\gamma_{max}$  taken at the same normalized radius in figure 8. It can be seen that  $\gamma_E$  increases faster than  $\gamma_{max}$ . At 9.8 s,  $\gamma_E$  is two times greater than  $\gamma_{max}$ , and it becomes four times greater at the end of the  $I_p$  plateau ( $t = 10.7 \text{ s}$ ). This could explain the experimental observations of turbulence and transport reductions, as suggested by the theoretical predictions of non-linear simulations and analytical approaches [28–30]. Experimental results confirming these predictions have been reviewed in ref. [31]. In spite of uncertainties in the value of  $\gamma_E$  (underestimated), it is likely that the rotation shear plays a stabilizing role, allowing the ITB to be maintained during the second flat-top.

#### 4. Stability analysis of a radiative improved confinement discharge on TEXTOR

On TEXTOR, the RI mode, characterized by good confinement at high density (up to 1.2 times the Greenwald limit) and high radiated power fraction, is routinely obtained by impurity seeding [5, 32, 33]. The RI discharges are obtained with co-injection neutral beam heating, with combined ICRH or counter-NBI. Experiments are performed at  $I_p = 0.4 \text{ MA}$ ,

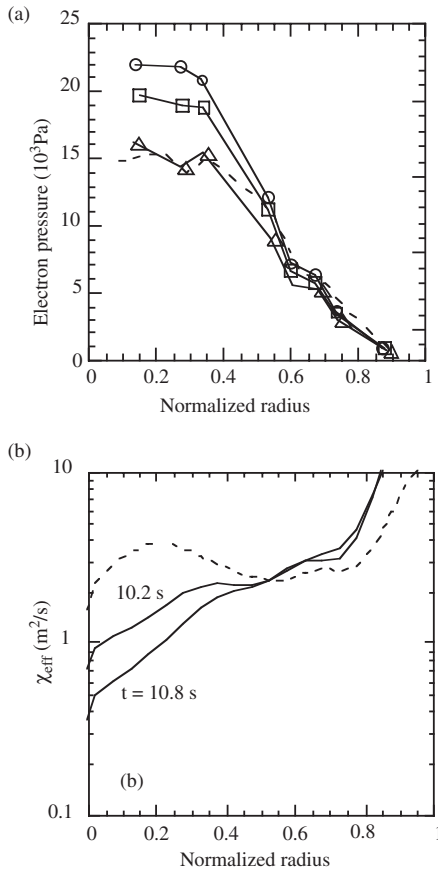


**Figure 4.** Evolution of radial profiles for discharge TS25196. (a) Electron pressure:  $t = 9.8 \text{ s}$  (triangles,  $P_{ICRH} = 2 \text{ MW}$ ),  $t = 10.2 \text{ s}$  (squares,  $P_{ICRH} = 4 \text{ MW}$ ) and  $t = 10.8 \text{ s}$  (circles,  $P_{ICRH} = 4 \text{ MW}$ ). The dashed curve corresponds to the reference L mode shot performed with  $P_{ICRH} = 4 \text{ MW}$ . (b) Effective electron heat diffusivity at  $t = 10.2$  and  $10.8 \text{ s}$  compared with the L mode reference discharge (dashed curve).

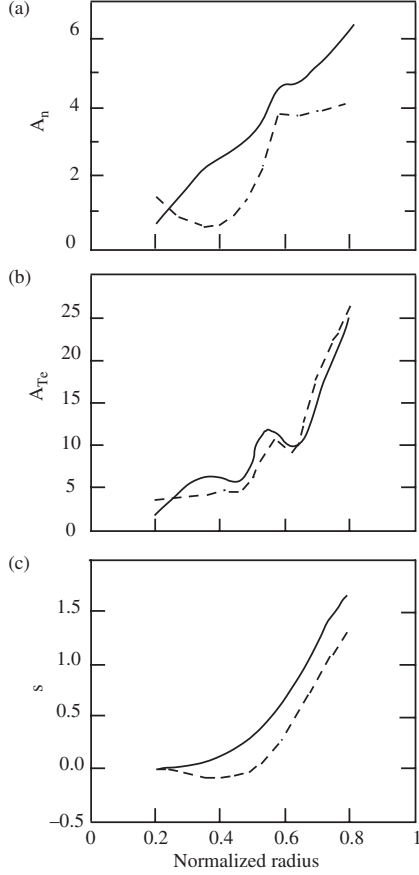


**Figure 5.** Radial profiles of different parameters for discharge TS25196 at  $t = 9.8$  s (solid curves) and  $t = 9.1$  s (dashed curves). (a) Normalized density gradient length  $A_n = R/L_n$ . (b) Normalized electron temperature gradient length  $A_T = R/L_T$ . (c) Magnetic shear  $s$ .

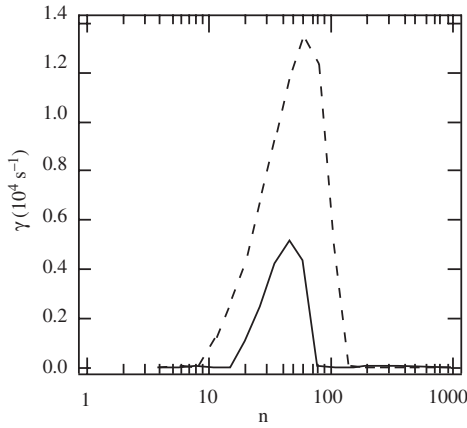


**Figure 6.** Stabilizing effect of negative magnetic shear. Growth rate spectra at  $r/a = 0.4$  for shot TS25195 at  $t = 9.1$  s. Solid curve: measured  $s = -0.1$ . Dashed curve: assuming  $s = 0.2$ .

$B_T = 2.25$  T, with a total injected power of up to 4 MW. Various impurities (argon, silicon or neon) are injected for plasma seeding, allowing a very high fraction of radiated power (up to 95%) to be achieved. In addition, the global confinement time is found to exceed the standard L mode prediction and reaches the value predicted for the ELM free H mode. Such a

regime generally exhibits the following features: a high level of impurity concentration and an increase in the peakedness of the density and temperature profiles.

This work is devoted to identifying the main mechanism responsible for this RI mode. For this purpose, we compare an RI discharge (68803) with an L mode reference discharge (68812) using deuterium as working gas. Both discharges were obtained with  $I_p = 400$  kA, with NBI power of 1.25 MW and ICRH power of 1.35 MW (figure 9), and with  $n_e(0) = 5.5 \times 10^{19} \text{ m}^{-3}$  in the RI case and  $n_e(0) = 5 \times 10^{19} \text{ m}^{-3}$  in the reference case. In the RI discharge, the density reaches up to 0.9 times the Greenwald limit and the radiated power up to 60% of the total injected power. In this plasma, neon was seeded. The line averaged value of the effective charge ( $Z_{eff}$ ) reaches 2.7. For the L mode plasma without neon injection, carbon was the main impurity, with  $Z_{eff} = 1.2$ . During the RI phase, both density and temperature profiles became more peaked, as shown in figure 10. The current density profile is almost the same for both discharges.

In our stability analysis, we first isolate the stabilizing effect of impurity seeding by including neon and carbon impurities for RI and L mode discharges, respectively. Then we investigate the stabilizing effect of rotation shear. No radial variation of  $Z_{eff}$  is taken into account. For the L mode discharge, the maximum value of the growth rate over each spectrum at each radius is plotted in figure 11 (dashed curve). In order to evaluate the effect of impurity seeding, KINEZERO is run imposing  $Z_{eff} = 2.7$  (which is the value obtained in the RI plasma) instead of the measured value of 1.2. The

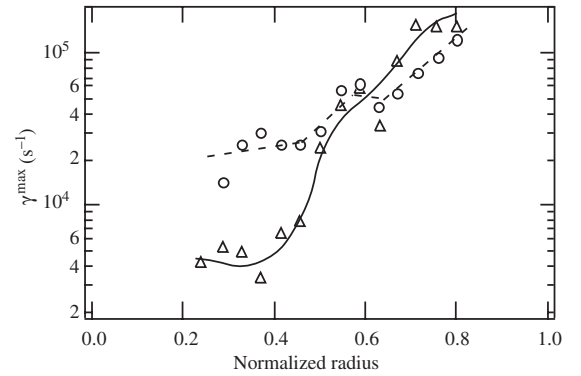


**Figure 7.** Radial profiles of maximum growth rates for shot TS25196 at  $t = 9.1$  s (triangles) and  $t = 9.8$  s (circles).

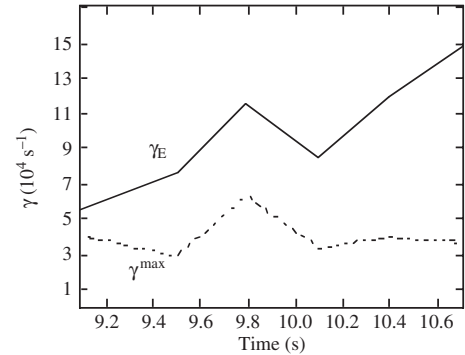


**Figure 8.** Time evolution of rotation shearing rate (solid curve) and maximum growth rate (dashed curve) at  $r/a = 0.6$  for shot 25196.

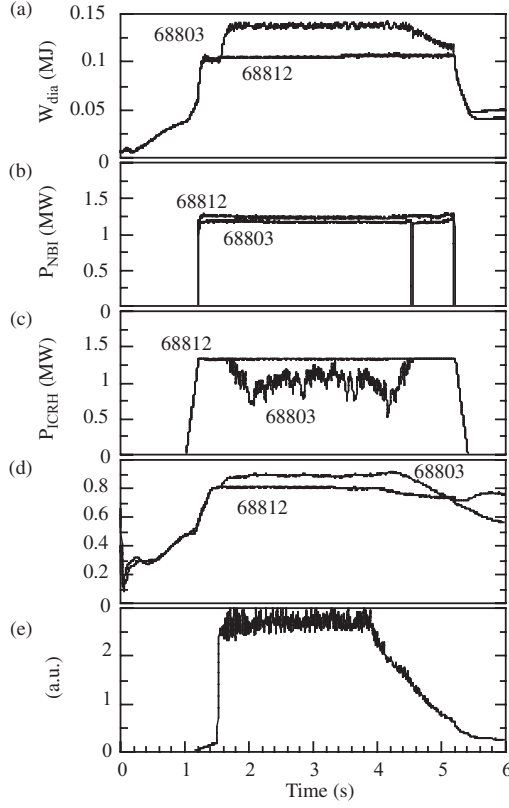


**Figure 9.** Comparison of two TEXTOR discharges with (68803, RI mode) and without (68812, L mode) neon injection. (a) Total energy from diamagnetic measurements. (b) Neutral beam power. (c) ICRH power. For shot 68803 a feedback control on  $P_{ICRH}$  was used to maintain  $W_{dia}$  at 0.14 MJ. (d) Density normalized to the Greenwald limit. (e) Brightness of neon VIII line for shot 68803.

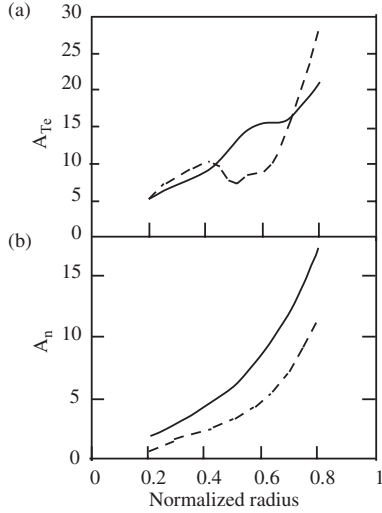


**Figure 10.** Radial profiles of normalized gradient lengths at  $t = 2.3$  s for RI (68803, solid curve) and L mode (68812, dashed curve) discharges: (a)  $A_T = R/L_T$ , (b)  $A_n = R/L_n$ .

result is shown in figure 11 (solid curve). The stabilizing effect of high  $Z_{eff}$  is consistent with the improved confinement observed in the RI discharge. In figure 12, two sets of spectra at  $r/a = 0.5$  and  $0.75$  are shown. On each the growth rates with  $Z_{eff} = 1.2$  are compared with the case where  $Z_{eff} = 2.7$ .

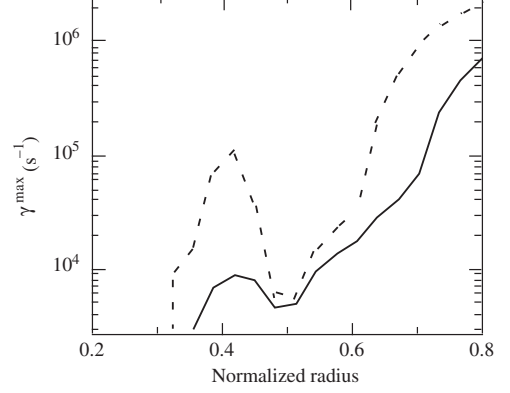


**Figure 11.** Stabilizing effect of  $Z_{eff}$ . Radial profiles of maximum growth rates for L mode discharge 68812 at  $t = 2.3$  s computed with measured  $Z_{eff} = 1.2$  (dashed curve) and with  $Z_{eff} = 2.7$  obtained in RI discharge 68803 (solid curve).

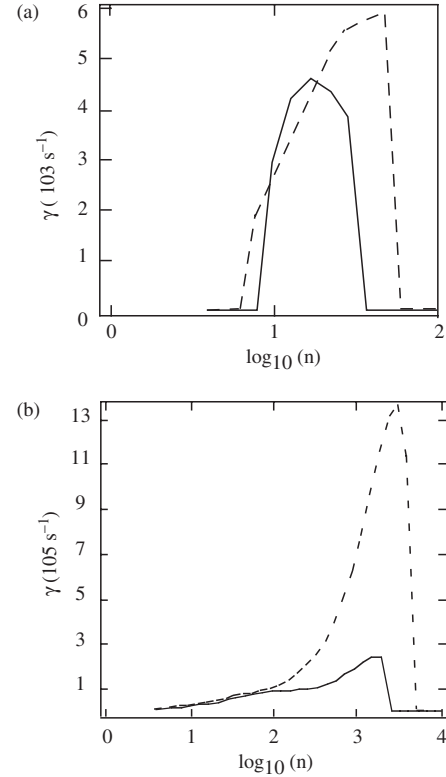


**Figure 12.** Stabilizing effect of  $Z_{eff}$ . Growth rates versus wavenumber for L mode discharge 68812 at  $t = 2.3$  s, (a)  $r/a = 0.5$  and (b)  $r/a = 0.75$ , computed with measured  $Z_{eff} = 1.2$  (dashed curve) and with  $Z_{eff} = 2.7$  obtained in RI discharge 68803 (solid curve).

A high value of  $Z_{eff}$  induces a significant reduction in the high wavenumber modes,  $n > 100$  (up to 85%), figure 12(b). Conversely, a reduction of about 25% is observed for lower wavenumber modes ( $n < 100$ ), figure 12(a). A similar behaviour has been observed in the stability analysis of the DIII-D improved confinement mode with neon injection [34] using the gyrokinetic code GS2 [11]. This global stabilizing effect of high  $Z_{eff}$  had previously been observed and reported in ref. [35]. The main physical reason for this effect is that impurity seeding at a given electron density is accompanied



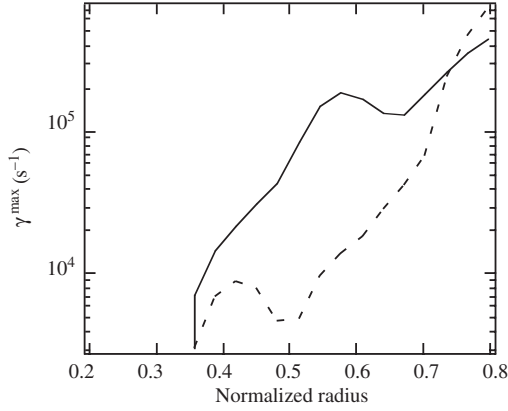


**Figure 13.** Effects of temperature and density peaking. Radial profiles of maximum growth rates for RI (68803, solid curve) and L mode (68812, dashed curve) discharges computed with  $Z_{eff} = 2.7$  obtained in 68803 at  $t = 2.3$  s.

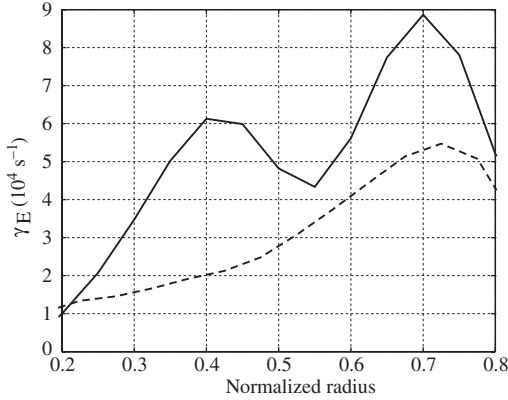


**Figure 14.** Radial profiles of rotation shearing rate at  $t = 2.3$  s. L mode discharge 68812 (dashed curve) and RI discharge 68803 (solid curve).

by dilution. This implies a decrease of the total ion pressure gradient, and therefore of the interchange drive. One exception to this general effect is that increasing  $Z_{eff}$  can be destabilizing for a flat density profile close to the stability threshold [37]. In the present case, since the density profile is peaked, the stabilizing effect through dilution is the dominant mechanism. This result is consistent with the result obtained by Tokar *et al* [37]. The strength of the  $Z_{eff}$  stabilizing effect follows the increases of the normalized temperature gradient profile, as shown in figure 10(b) (dashed curve).

For the RI discharge 68803, after the onset of the stabilizing effect of the impurity, the density and temperature gradients simultaneously increase during the improved confinement phase (figure 10). This induces an increase in  $\gamma_{max}$  compared with the value of the L mode discharge, as shown in figure 13. Here the collisions are neglected although the electron effective collision frequency is 2 to 10 times larger than the electron vertical drift frequency (for  $0.5/\rho_i < k_\theta < 0.1/\delta_e$ ,  $\rho_i$  being the ion Larmor radius and  $\delta_e$  being the electron banana width). The neglected dissipative electron drift mode belongs to the same branch as the computed collisionless TEM. The main effect of collisions on the TEM is to diminish its growth rate. Also, the stabilizing effect due to density peaking that occurs when trapped electrons are taken adiabatic does

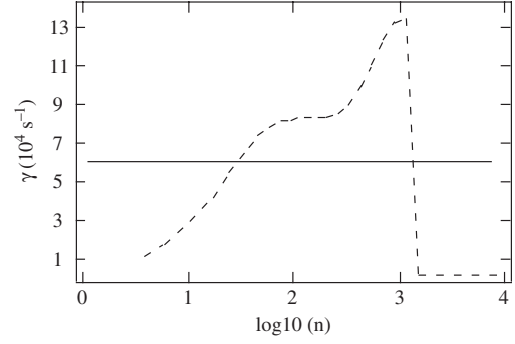


**Figure 15.** Growth rate versus  $n$  for RI discharge 68803 (dashed curve) compared with rotation shearing rate (solid line), at  $t = 2.3$  s and  $r/a = 0.6$ .

not appear here. In fact, we find that the stabilizing effect of the density gradient is rather weak, as expected for a kinetic ITG/TEM close to the threshold [38]. Therefore neglecting collisions in the TEXTOR RI mode is equivalent to neglecting two stabilizing factors—collisionality and density peaking—leading to overestimated growth rates. Despite this major limitation, we stay on the safe side for comparing the  $\mathbf{E} \times \mathbf{B}$  shear rate with the growth rate. The rotation shearing rate is evaluated with a radial electric field deduced from neoclassical calculations performed with NCLASS [39] and based on the measured toroidal velocity profile. The radial profile of  $\gamma_E$  for both RI and L mode is shown in figure 14. For  $n < 60$ , the growth rates at  $r/a = 0.6$  are found to be lower than  $\gamma_E$  (figure 15). The RI mode analysed is heated by co-NBI. The role of the  $\mathbf{E} \times \mathbf{B}$  shear is certainly less important in RI modes obtained with balanced NBI.

## 5. Summary

A fast, reliable stability code, called KINEZERO, that produces growth rate spectra at each radius has been developed at Tore Supra. It is based on a variational principle using a set of simplified gyrokinetic equations with linear, electrostatic and collisionless approximations. Typically the computational time is a few hours on a Dec Alpha workstation: five hours to explore the plane  $(n, r/a)$  for about 50 time slices and 20 radial positions. This code has been routinely used to analyse various experiments. In particular, the main mechanisms responsible for two types of improved plasma on Tore Supra (ITB) and TEXTOR (RI mode) have been identified.

For Tore Supra experiments, ITBs are found to be triggered by a central negative magnetic shear. The ITBs are then maintained in quasi-steady state (the current density relaxes to a monotonic profile) by an increase of the  $\mathbf{E} \times \mathbf{B}$  shear rate, which exceeds the maximum growth rates. For RI modes in TEXTOR, the impurity seeding is globally stabilizing and thus triggers the improvement. The increase of rotation shear is found to be the main parameter allowing the improved confinement to be maintained, which is similar to the ITB case in Tore Supra.

## Appendix A. Main outline of the model

We are interested here in electrostatic microinstabilities; the magnetic perturbations are neglected. The instabilities are

characterized by their growth rates ( $\gamma$ ). To calculate them, one has to compute the perturbed distribution function distribution ( $\tilde{f}$ ) coupled to the electrostatic perturbations ( $\tilde{\phi}$ ) via the Vlasov equation and express the electroneutrality constraint via the Maxwell equations. Here we neglect the effect of collisions. The perturbed electrostatic potential is expressed using a Gaussian trial function in the lowest order ballooning representation. The perturbation frequencies, solutions of the computed equation, are evaluated using a generalized Nyquist method.

#### Appendix A.1. Perturbed Vlasov equation

If one supposes that the growth time ( $\gamma^{-1}$ ) and the spatial scales of the perturbations are smaller than the equilibrium evolution time and the gradient lengths, and that the amplitude of the perturbations ( $\tilde{f}$ ,  $\tilde{\phi}$ ) is lower than the values at equilibrium ( $f_0$ ,  $\phi_0$ ), then one can write

$$\begin{aligned}\phi &= \phi_0 + \tilde{\phi} \\ f &= f_0 + \tilde{f}\end{aligned}\quad (5)$$

with

$$\begin{aligned}\tilde{\phi}(\mathbf{J}, \vartheta, t) &= \sum_{n\omega} \tilde{\phi}_{n\omega}(\mathbf{J}) e^{i(n\cdot\vartheta - \omega t)} \\ \tilde{f}(\mathbf{J}, \vartheta, t) &= \sum_{n\omega} \tilde{f}_{n\omega}(\mathbf{J}) e^{i(n\cdot\vartheta - \omega t)}.\end{aligned}\quad (6)$$

( $\vartheta$ ,  $\mathbf{J}$ ) is a set of angular and action variables. The evident radial, poloidal and toroidal geometric co-ordinates ( $r$ ,  $\theta$ ,  $\varphi$ ) are periodic functions of  $\vartheta$ .

The linearized Vlasov equation is expressed as follows:

$$\tilde{f}_{n\omega}^s = -e_s \frac{f_0^s}{T_s} \left( 1 - \frac{\omega - \mathbf{n} \cdot \boldsymbol{\omega}_s^*}{\omega - \mathbf{n} \cdot \boldsymbol{\Omega}} \right) \tilde{\phi}_{n\omega} \quad (7)$$

where the equilibrium distribution function is a Maxwellian:

$$f_0^s = \frac{n_s}{(2\pi m_s T_s)^{3/2}} e^{-E/T_s}.$$

With  $e_s$ ,  $m_s$ ,  $T_s$  and  $n_s$  the charge, mass, temperature and density of species  $s$ .  $E$  is their kinetic energy.  $\boldsymbol{\Omega}$  is such that

$$\boldsymbol{\Omega} = \frac{\partial \vartheta}{\partial t}.$$

$\omega_s^*$ , called the diamagnetic drift frequency, is such that

$$\omega_s^* = T_s \left[ \frac{\partial \ln(n_s)}{\partial \mathbf{J}} + \left( \frac{E_{cs}}{T_s} - \frac{3}{2} \right) \frac{\partial \ln(T_s)}{\partial \mathbf{J}} \right].$$

#### Appendix A.2. Electroneutrality

For fluctuating scales greater than the Debye length the self-consistency is ensured by the electroneutrality constraint

$$\sum_s e_s \tilde{n}_s = 0. \quad (8)$$

The variational approach gives another expression for the electroneutrality [17]:

$$\sum_s \mathcal{L}_s(\omega) = 0 \quad (9)$$

with

$$\mathcal{L}_s(\omega) = - \sum_{n,\omega} \int e_s \tilde{n}_{n,\omega}^s(\mathbf{x}) \tilde{\phi}_{n,\omega}^*(\mathbf{x}) d^3 \mathbf{x}. \quad (10)$$

Combining equation (10) with equation (7), one obtains the equation driving the electrostatic potential perturbations, from which we want to deduce the growth rates:

$$\begin{aligned}\sum_s \frac{e_s^2 f_0^s}{T_s} \left[ \sum_n \langle \tilde{\phi}_{n,\omega} \tilde{\phi}_{n,\omega}^* \rangle \right. \\ \left. - \sum_n \left\langle \frac{\omega - \mathbf{n} \cdot \boldsymbol{\omega}_s^*}{\omega - \mathbf{n} \cdot \boldsymbol{\Omega}} \tilde{\phi}_{n,\omega} \tilde{\phi}_{n,\omega}^* \right\rangle \right] = 0\end{aligned}\quad (11)$$

where  $\langle \dots \rangle = \int d^3 \vartheta \int d^3 \mathbf{J} \dots$

We want to express the perturbed electrostatic potential in the variables ( $r$ ,  $\theta$ ,  $\varphi$ ). The intrinsic periodicity with respect to  $\theta$  and  $\varphi$  allows us to decompose  $\tilde{\phi}$  in Fourier series such that

$$\tilde{\phi}_{n,\omega}(\mathbf{J}) = \int_0^{2\pi} \frac{d^3 \vartheta}{(2\pi)^3} \tilde{\phi}(r, \theta, \varphi, t) e^{-in\cdot\vartheta} \quad (12)$$

with

$$\tilde{\phi}(r, \theta, \varphi, t) = \sum_{mn,\omega} \tilde{\phi}_{mn,\omega}(r) e^{i(m\theta + n\varphi - \omega t)}. \quad (13)$$

$m$  and  $n$  are the poloidal and toroidal wavenumbers, respectively.

In a torus the axisymmetry imposes  $e^{in\varphi}$  as an eigenvector. In contrast, in the poloidal direction there is no axisymmetry as the magnetic field varies with  $\theta$ . Therefore the search for the eigenvectors  $\tilde{\phi}_{mn,\omega}(r)$  at given  $n$  is a 2-D problem. The micro-instabilities are characterized by a spatial extension that is much greater parallel to the magnetic field line than perpendicular to it:  $k_{\parallel} \ll k_{\perp}$ . The ballooning representation uses this property to bring the problem back to one dimension [40–42, 27].

In this representation we rewrite  $\tilde{\phi}(r, \theta, \varphi, t)$  as follows:

$$\begin{aligned}\tilde{\phi}(r, \theta, \varphi, t) &= \sum_{n,\omega} \int \frac{d\theta_0}{2\pi} \sum_{l=-\infty}^{+\infty} \hat{\phi}_{n\omega\theta_0}(\theta + 2\pi l) \\ &\times \exp\{i[n(\varphi - q(r)(\theta + 2\pi l - \theta_0)) - \omega t]\}.\end{aligned}\quad (14)$$

The sum over  $l$  maintains the periodicity in  $\theta$ . The modes are said to be ballooned around the ballooning angle  $\theta_0$ . Here we choose  $\theta_0 = 0$ . We then obtain

$$\begin{aligned}\tilde{\phi}_{mn,\omega}(r) &= \int \frac{d\theta d\varphi d(\omega_0 t)}{(2\pi)^3} \tilde{\phi}(r, \theta, \varphi, t) e^{-im\theta} e^{-in\varphi} e^{i\omega t} \\ &= \int \frac{d\theta}{2\pi} \hat{\phi}_{n\omega}(\theta) e^{-i(nq(r)+m)\theta}.\end{aligned}\quad (15)$$

The lowest order of the ballooning representation is used. We write

$$q(r) \simeq q(r_0) + x \partial_r q|_{r_0} \quad (16)$$

with  $r_0$  the radius associated with the resonating surface such that  $q(r_0) = -m_0/n$ ;  $x$  is the distance to this surface. Therefore  $r = r_0 + x$ , and  $d$  is the distance between two resonating surfaces:  $d = -1/n \partial_r q$ .

Making the variables change,  $\theta = kd$ , one obtains

$$\tilde{\phi}_{mn,\omega}(r) = \int |d| \frac{dk}{2\pi} \hat{\phi}_{n\omega r_0}(kd) e^{ikd((x/d)-v)}. \quad (17)$$

Finally,  $\tilde{\phi}_{mn,\omega}(r)$  is an infinite sum of identical modes for each pair ( $n$ ,  $r_0$ ).



This limit is no longer valid when the first derivative of an equilibrium quantity is zero, as in this case the second derivative is not negligible. In particular, the plasmas in which the magnetic shear is zero are not properly represented by the lowest order ballooning representation.

### Appendix A.3. Choice for the electrostatic potential

In order to find quickly a growth rate spectrum at each radius, we choose a trial function for the fluctuating electrostatic potential. In our variational approach,  $\tilde{\phi}$  is chosen to be the most unstable exact solution obtained in the fluid limit for strongly ballooned modes, so

$$\tilde{\phi}(k_r) = \phi_0 \frac{w^{1/2}}{\pi^{1/4}} e^{-k_r^2 w^2/2} \quad (18)$$

in order to find

$$\int_{-\infty}^{+\infty} \frac{dk_r}{2\pi} |\tilde{\phi}(k_r)|^2 = \int_{-\infty}^{+\infty} dx |\tilde{\phi}(x)|^2 = \phi_0^2.$$

The mode width ( $w$ ) is calculated in the fluid limit as well, in the case where the interchange is the dominant instability:

$$w^4 = \frac{f_i \frac{q^2}{2\epsilon} \sum_s J_0^2(k_\theta \rho_{cs}) \frac{T_s m_s}{Z_s^2 e^2 B^2}}{f_p \frac{R}{L_s^2} \sum_s J_0^2(k_\theta \rho_{cs}) \frac{T_s e^2 B^2}{m_s} \frac{\sum_s n_s (Z_s^2 / T_s)}{\sum_s n_s (T_s / L_{ps})}} \quad (19)$$

with  $1/L_{ps} = -\nabla P_s / P_s$ ,  $1/L_s = \nabla q / q$ ,  $f_i$  and  $f_p$  being the fractions of trapped and passing particles, respectively.

If  $k_\theta \rho_{cs} \gg 1$ , the species  $s$  becomes adiabatic ( $J_0^2(k_\theta \rho_{cs}) \rightarrow 0$ ). The mode width then scales as the species which remains resonant. It should also be noted that when  $s$  goes to zero, the mode width diverges to infinity. To avoid this, the mode width is artificially limited to a tenth of the minor radius.

### Appendix A.4. Computed form

Combining the perturbed Vlasov equation with the variational form of electroneutrality, one obtains an equation from which  $\omega$  is a solution such that

$$\mathcal{D}(\omega) = \sum_s \frac{n_s Z_s^2}{T_s} [1 - \mathcal{L}_{ts}(\omega) - \mathcal{L}_{ps}(\omega)] = 0. \quad (20)$$

**Appendix A.4.1. Trapped particles.** For trapped particles, the functional can be written as follows:

$$\mathcal{L}_{ts}(\omega) = \left\langle \int \frac{dk_r}{2\pi} J_0^2(k_\perp \rho_{cs}) J_0^2(k_r \delta_s) \times \frac{\omega - n\omega_s^*}{\omega - n\omega_{ds} + i0^+} |\tilde{\phi}(k_r)|^2 \right\rangle_t. \quad (21)$$

$J_0(k_\perp \rho_{cs})$  is the Bessel function standing for the gyro-average over the cyclotron motion. The bounce average for trapped particles is also expressed by a Bessel function,  $J_0^2(k_r \delta_s)$ . As the trapped particles are mainly efficient at low wavenumbers, we suppose that  $n \ll k_r / \pi \partial q$ ; therefore  $k_r d \gg \pi$ .

The integration domain is as follows:

$$\langle \dots \rangle_t = \int_0^{+\infty} \frac{2}{\sqrt{\pi}} \sqrt{\mathcal{E}} e^{-\mathcal{E}} d\mathcal{E} \int_{\lambda_c}^1 \frac{d\lambda}{4\bar{\omega}_2} \dots$$

$$= f_t \int_0^{+\infty} \frac{2}{\sqrt{\pi}} \sqrt{\mathcal{E}} e^{-\mathcal{E}} d\mathcal{E} \int_0^1 K(\kappa) \kappa d\kappa \dots$$

$\mathcal{E}$  is such that  $\mathcal{E} = E / T_s$ ,  $\kappa$  is such that  $\lambda = 1 - 2\epsilon\kappa^2$ . The vertical drift frequency is given by

$$n\omega_{ds} = -\frac{k_\theta T_s}{e_s B R} f(\kappa) \mathcal{E}$$

with

$$f(\kappa) = 2 \frac{E(\kappa)}{K(\kappa)} - 1 + 4s \left[ \kappa^2 - 1 + \frac{E(\kappa)}{K(\kappa)} \right].$$

$K$  and  $E$  are the complete elliptic integrals of the first and second kinds.

As we are working with Maxwellian distribution functions, the main part of the particles have an energy around the thermal value. Using this property, we separate the energy integration of the Bessel functions from the rest as follows:

$$\int_0^{+\infty} \frac{2}{\sqrt{\pi}} \sqrt{\mathcal{E}} e^{-\mathcal{E}} d\mathcal{E} J_0^2(a\mathcal{E}) = e^{-a^2} I_0(a^2) = \mathcal{B}(a). \quad (22)$$

Therefore

$$\mathcal{L}_{ts}(\omega) \simeq \left\langle \frac{\omega - n\omega_s^*}{\omega - n\omega_{ds}} \right\rangle_t \mathcal{B}(k_\perp \rho_{cs}^{th}) \mathcal{B}(k_r \delta_s^{th}) \quad (23)$$

with

$$\mathcal{B}(k_\perp \rho_{cs}^{th}) \mathcal{B}(k_r \delta_s^{th}) \simeq \mathcal{B}(k_\theta \rho_{cs}^{th}) \mathcal{B}(k_r \delta_s^{th}).$$

As  $\rho_{cs}^{th} \ll \delta_s^{th}$ , the main radial width for trapped particles is the banana width.

We can then rewrite  $\mathcal{L}_{ts}$  to express the energy integration under the form of Fried and Conte integrals:

$$\mathcal{L}_{ts}(\omega) \simeq \left\langle \frac{\Omega \frac{Z_s}{\tau_s f(\kappa)} - \left[ \frac{A_{ns}}{f(\kappa)} + \frac{A_{Ts}}{f(\kappa)} (\mathcal{E} - 3/2) \right]}{\Omega \frac{Z_s}{\tau_s f(\kappa)} - \mathcal{E}} \right\rangle_t$$

$$\times \mathcal{B}(k_\theta \rho_{cs}^{th}) \mathcal{B}(k_r \delta_s^{th}) \quad (24)$$

with  $\Omega = \omega(RBe/k_\theta \bar{T})$ ,  $A_{ns} = R/L_{ns}$ ,  $A_{Ts} = R/L_{Ts}$  and  $e_s = Z_s e$ ,  $T_s = \tau_s \bar{T}$  ( $\bar{T} = 1$  keV). The integration with respect to  $\kappa$  is done numerically.

**Appendix A.4.2. Passing particles.** For passing particles, the functional can be written as follows [17]:

$$\mathcal{L}_{ps}(\omega) = \left\langle -id \frac{\omega - \omega_s^*}{|\omega_2|} \int \int_{-\infty}^{+\infty} \frac{d\bar{\varphi}_2 d\bar{\varphi}_2'}{2\pi} Y \left( \frac{\bar{\varphi}_2' - \bar{\varphi}_2}{\omega_2} \right) \times J_0[k_\perp(\bar{\varphi}_2) \rho_{cs}] \tilde{\phi}(\bar{\varphi}_2) J_0[k_\perp(\bar{\varphi}_2') \rho_{cs}] \tilde{\phi}^*(\bar{\varphi}_2') \right\rangle_p = 0. \quad (25)$$

$Y$  stands for the Heaviside function.

We have supposed  $k_r d \ll \pi$ ; therefore  $n \gg k_r / (\pi \nabla q)$  and  $\bar{\varphi}_2 = k_r d$ . The integration domain is as follows:

$$\langle \dots \rangle_p = \int_0^{+\infty} \frac{2}{\sqrt{\pi}} \sqrt{\mathcal{E}} e^{-\mathcal{E}} d\mathcal{E} \int_0^{\lambda_c} \frac{d\lambda}{4\bar{\omega}_2} \frac{1}{2} \sum_{\epsilon_l} \dots$$

and

$$\bar{\varphi}_2 = kd(\bar{\varphi}'_2 = k'd) \quad \text{with } d = -\frac{1}{n\partial_r q}$$

$$\hat{\phi}(k) = \int_{-\infty}^{+\infty} dx e^{-ikx} \phi(x) \quad (\text{identical to } x' \text{ and } k').$$

The integration over  $\lambda$  is not done exactly, so  $k_{\parallel} V_{\parallel} = \langle k_{\parallel} V_{\parallel} \rangle_{\lambda}$  and  $n\omega_{gs} = \langle n\omega_{gs} \rangle_{\lambda}$ , such that for high values of  $\omega$  we match the fluid form of the equation.

- (a) The transit frequency along magnetic field lines is defined by  $k_{\parallel} V_{\parallel} = k_{\parallel} \bar{V}_{\parallel} \rho^* \sqrt{\mathcal{E}} \epsilon_{\parallel}$ , with  $\epsilon_{\parallel} = \pm 1$  and

$$k_{\parallel} \bar{V}_{\parallel} = -\frac{w}{d} \frac{V_{Ts}}{qR} \frac{1}{\sqrt{3}}.$$

- (b) The vertical drift frequency is such that:  $n\omega_{gs} = n\bar{\omega}_{gs} \mathcal{E} f(k^*)$ , with

$$n\bar{\omega}_{gs} = -\frac{k_{\theta} T_s}{Z_s e B} \frac{1}{R}$$

and

$$f(k^*) = \frac{4}{3} \cos\left(k^* \frac{d}{w}\right) + sk^* \frac{d}{w} \sin\left(k^* \frac{d}{w}\right).$$

We finally obtain

$$\mathcal{L}_{ps}(\omega) = \left\langle \int_{-\infty}^{+\infty} dx \phi(x)^2 \frac{\omega - n\omega_s^*}{\omega - n\omega_{gs} - k_{\parallel} V_{\parallel} + i0^+} \right\rangle_p \times \mathcal{B}(k_{\perp} \rho_{cs}^{th}). \quad (26)$$

We rewrite  $\mathcal{L}_{ps}$  in order to identify the analytical form of the integration with respect to  $\mathcal{E}$ :

$$\begin{aligned} \mathcal{L}_{ps}(\omega) &\simeq \int_{-\infty}^{+\infty} \frac{d\rho^*}{\sqrt{\pi}} e^{-\rho^{*2}} \int_{-\infty}^{+\infty} \frac{dk^*}{\sqrt{\pi}} e^{-k^{*2}} \\ &\times \left[ \left( \frac{-\omega}{n\bar{\omega}_{gs}} + \frac{n\omega_{ns}^*}{n\bar{\omega}_{gs}} - \frac{3}{2} \frac{n\omega_{Ts}^*}{n\bar{\omega}_{gs}} \right) \mathcal{I}_s(k^*, \rho^*) \right. \\ &\left. + \frac{n\omega_{Ts}^*}{n\bar{\omega}_{gs}} \mathcal{J}_s(k^*, \rho^*) \right] \mathcal{B}(k_{\perp} \rho_{cs}^{th}). \end{aligned} \quad (27)$$

$\mathcal{I}_s$  and  $\mathcal{J}_s$  are combinations of the Fried and Conte integrals such that

$$\begin{aligned} \mathcal{I}_s(k^*, \rho^*) &= \frac{1}{2} \sum \epsilon_{\parallel} \frac{1}{f(k^*)} \int_0^{+\infty} \frac{2}{\sqrt{\pi}} \sqrt{\mathcal{E}} e^{-\mathcal{E}} d\mathcal{E} \\ &\times \frac{1}{\mathcal{E} + \frac{k_{\parallel} \bar{V}_{\parallel} \rho^* \epsilon_{\parallel}}{n\bar{\omega}_{gs} f(k^*)} \sqrt{\mathcal{E}} + \frac{-\omega}{n\bar{\omega}_{gs} f(k^*)}} \end{aligned} \quad (28)$$

and

$$\begin{aligned} \mathcal{J}_s(k^*, \rho^*) &= \frac{1}{2} \sum \epsilon_{\parallel} \frac{1}{f(k^*)} \int_0^{+\infty} \frac{2}{\sqrt{\pi}} \mathcal{E}^{3/2} e^{-\mathcal{E}} d\mathcal{E} \\ &\times \frac{1}{\mathcal{E} + \frac{k_{\parallel} \bar{V}_{\parallel} \rho^* \epsilon_{\parallel}}{n\bar{\omega}_{gs} f(k^*)} \sqrt{\mathcal{E}} + \frac{-\omega}{n\bar{\omega}_{gs} f(k^*)}} \end{aligned} \quad (29)$$

The double integration with respect to  $\rho^*$  and  $k^*$  is done numerically.

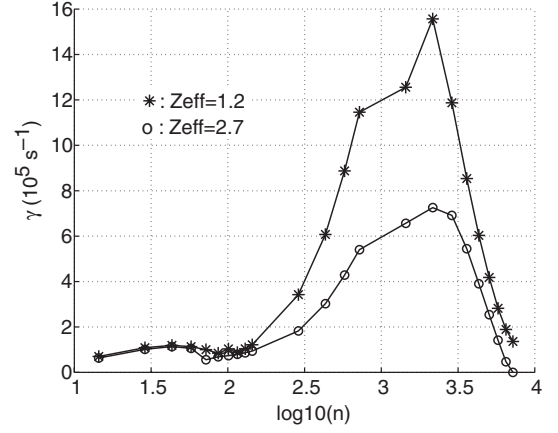


**Figure 16.** Same case as in figure 12(b) but using the gyrokinetic code GS2. TEXTOR discharge 68812 at  $t = 2.3$  s,  $r/a = 0.75$  with measured  $Z_{eff} = 1.2$  (asterisks) and with  $Z_{eff} = 2.7$  obtained in RI discharge 68803 (circles).

#### Appendix A.5. Validation

The generalized Nyquist method has been tested to find known polynomial roots in the complex plane. The expected symmetry in the equations has also been tested. For example, the same results have been found with trapped particles only and with passing particles only with the finite banana width effect neutralized for trapped particles, the transit frequency of the passing particles brought to zero and the vertical drift multiplicative terms  $f(\kappa)$  for trapped particles and  $f(k^*)$  for passing particles forced to be equal to 1. The same results were found for electrons only and for ions only, where the mass of the ions was artificially set to the mass of the electrons. The exercise was also done for impurities only and main ions only. The last test was done with trapped electrons only and trapped ions only, with  $T_e = T_i$  and  $n_e = n_i$ . The finite Larmor radius effects were not included, such that the mass of each species does not come into play. In this case, the dispersion relation becomes symmetric such that if  $\omega$  is a solution then  $-\omega^*$  must also be a solution. This is what was found. Therefore the implementation of electrons, main ions and impurities has been checked with respect to each other, as well as passing versus trapped particles. Before showing any benchmarking results, it should be noted here that the choices made to have a fast code are not compatible with a perfect quantitative agreement with respect to a gyrokinetic code that solves the eigenfunctions self-consistently. Nevertheless, in figure 16, figure 12(b) is reproduced using the gyrokinetic code GS2 [11]. By comparing the two figures, one can observe a good qualitative agreement: the stabilizing effect of impurities is stronger for the ETG branch. The quantitative agreement is also good except for the ETG part of the spectrum of the case with  $Z_{eff} = 2.7$ , where the GS2 growth rates are higher than the KINEZERO growth rates.

#### Acknowledgments

The authors wish to express their appreciation for the diligent support of the Tore Supra team. Useful discussions with A. Messiaen on the RI mode in TEXTOR are gratefully

acknowledged. The authors thank W. Dorland for allowing them to use GS2.

## References

- [1] Levinton F.M. *et al* 2000 *Phys. Rev. Lett.* **84** 3097
- [2] Strait E.J. *et al* 1995 *Phys. Rev. Lett.* **75** 4421
- [3] Ishida S. *et al* 1997 *Phys. Rev. Lett.* **79** 3917
- [4] Gormezano C. *et al* 1998 *Phys. Rev. Lett.* **80** 5544
- [5] Ongena J. *et al* 1993 *Nucl. Fusion* **33** 283
- [6] Buratti P. *et al* 1999 *Phys. Rev. Lett.* **82** 560
- [7] Günter S. *et al* 2000 *Phys. Rev. Lett.* **84** 3097
- [8] Hoang G.T. *et al* 2000 *Phys. Rev. Lett.* **84** 4593
- [9] Garbet X. *et al* 2001 *Phys. Plasmas* **8** 4267
- [10] Rewoldt G. *et al* 1982 *Phys. Fluids* **25** 480
- [11] Kotschenreuther M. *et al* 1995 *Comput. Phys. Commun.* **88** 128
- [12] Kotschenreuther M. *et al* 1995 *Phys. Plasmas* **2** 2381
- [13] Beer M.A. and Hammett G.W. 1996 *Phys. Plasmas* **3** 4046
- [14] Waltz R.E. *et al* 1997 *Phys. Plasmas* **4** 2482
- [15] Tang W.M., Connor J.W. and Hastie R.J. 1980 *Nucl. Fusion* **20** 1439
- [16] Rewoldt G. *et al* 1987 *Phys. Fluids* **30** 807
- [17] Garbet X. *et al* 1990 *J. Comput. Phys.* **87** 249
- [18] Davies B. 1986 *J. Comput. Phys.* **66** 36
- [19] Brunner S. *et al* 1998 *Phys. Plasmas* **5** 3929
- [20] Antar G. *et al* 2001 *Phys. Plasmas* **8** 186
- [21] Hahn T.S. and Burrell K.H. 1995 *Phys. Plasmas* **2** 1648
- [22] Stringer T.E. 1972 *Plasma Phys.* **14** 1063
- [23] Connor J.W. and Hastie R.J. 1973 *Nucl. Fusion* **13** 221
- [24] Yushmanov P.N. 1982 *Nucl. Fusion* **22** 1199
- [25] Shaing K.C. and Callen J.D. 1983 *Phys. Fluids* **26** 3315
- [26] Shaing K.C. *et al* 1998 *Phys. Rev. Lett.* **80** 5353
- [27] Romannikov A. *et al* 2000 *Nucl. Fusion* **40** 319
- [28] Waltz R.E. *et al* 1994 *Phys. Plasmas* **1** 2229
- [29] Biglari H., Diamond P. and Terry P.W. 1990 *Phys. Fluids B* **2** 1
- [30] Hamaguchi S. and Horton W. 1992 *Phys. Fluids B* **4** 319
- [31] Burrell K.H. 1997 *Phys. Plasmas* **4** 319
- [32] Messiaen A.M. *et al* 1994 *Nucl. Fusion* **34** 825
- [33] Vandenplas P.E. *et al* 1998 *J. Plasma Phys.* **59** 587
- [34] Staebler G.M. *et al* 1999 *Phys. Rev. Lett.* **82** 1692
- [35] Dominguez R.R. and Rosenbluth M.N. 1989 *Nucl. Fusion* **29** 844
- [36] Paccagnella R., Romanelli F. and Briguglio S. 1990 *Nucl. Fusion* **30** 545
- [37] Tokar' M.Z. *et al* 2000 *Phys. Rev. Lett.* **84** 895
- [38] Romanelli F. and Briguglio S. 1990 *Phys. Fluids B* **2** 754
- [39] Houlberg W.A. *et al* 1997 *Phys. Plasmas* **4** 3231
- [40] Samain A. 1970 *Proc. 4th Eur. Conf. on Controlled Fusion and Plasma Physics (Rome, 1970)* vol 1 (Geneva: European Physical Society) p 145
- [41] Taylor J.B. 1977 *Proc. 6th Int. Conf. on Plasma Physics and Controlled Nuclear Fusion Research (Berchtesgaden, 1976)* vol 2 (Vienna: IAEA) p 323
- [42] Connor J.W. *et al* 1993 *Phys. Rev. Lett.* **70** 1803.